Engineering of Intrinsic Chiral Torques in Magnetic Thin Films Based on the Dzyaloshinskii-Moriya Interaction

Zhentao Liu, Zhaochu Luo, Stanislas Rohart, Laura J Heyderman, Pietro Gambardella, Aleš Hrabec

Engineering of Intrinsic Chiral Torques in Magnetic Thin Films Based on the Dzyaloshinskii-Moriya Interaction

Zhentao Liu[1,2,*] Zhaochu Luo[1,2] Stanislas Rohart[3] Laura J. Heyderman[1,2]
Pietro Gambardella[4] and Aleš Hrabec[1,2,4,†]

[1] *Laboratory for Mesoscopic Systems, Department of Materials, ETH Zurich, 8093 Zurich, Switzerland*
[2] *Laboratory for Multiscale Materials Experiments, Paul Scherrer Institute, 5232 Villigen, Switzerland*
[3] *Université Paris-Saclay, CNRS, Laboratoire de Physique des Solides, 91405 Orsay, France*
[4] *Laboratory for Magnetism and Interface Physics, Department of Materials, ETH Zurich, 8093 Zurich, Switzerland*

(Received 9 July 2021; revised 9 September 2021; accepted 4 November 2021; published 29 November 2021)

The establishment of chiral coupling in thin magnetic films with inhomogeneous anisotropy has led to the development of artificial systems of fundamental and technological interest. The chiral coupling itself is enabled by the Dzyaloshinskii-Moriya interaction (DMI) enforced by the patterned noncollinear magnetization. Here, we create a domain wall track with out-of-plane magnetization coupled on each side to a narrow parallel strip with in-plane magnetization. With this we show that the chiral torques emerging from the DMI at the boundary between the regions of noncollinear magnetization in a single magnetic layer can be used to bias the domain wall velocity. To tune the chiral torques, the design of the magnetic racetracks can be modified by varying the width of the tracks or the width of the transition region between noncollinear magnetizations, reaching effective chiral magnetic fields of up to 7.8 mT. Furthermore, we show how the magnitude of the chiral torques can be estimated by measuring asymmetric domain wall velocities, and demonstrate spontaneous domain wall motion propelled by intrinsic torques even in the absence of any external driving force.

DOI: 10.1103/PhysRevApplied.16.054049

I. INTRODUCTION

The engineering of magnetic torques in magnetic nanostructures is central to the development of spintronic devices for nonvolatile information storage [1–6], Boolean logic [7–10], and neuro-inspired computation [11–13]. Magnetic torques can be induced by electric currents [1,3] or by coupling to a nearby magnetic layer, for example via the Ruderman-Kittel-Kasuya-Yosida interaction [6,14], the exchange interaction [15,16], and the dipolar interaction [17]. The implementation of interlayer coupling effects into magnetic devices has led to enhanced device performance, such as improved thermal stability [18–20], lower power consumption, and higher operating speed [21–25]. However, magnetic torques resulting from interlayer coupling offer limited possibilities for the operation of magnetic elements lying in the same plane, such as those found in planar magnetic logic circuits [9,26] and artificial spin ice systems [27]. The possibility of inducing intralayer coupling between adjacent nanomagnets offered by the interfacial Dzyaloshinskii-Moriya interaction (DMI) therefore opens alternative perspectives in this respect. Indeed, in recent work performed on DMI-coupled systems, a number of phenomena arising from the lateral coupling have been demonstrated, such as lateral exchange bias between adjacent regions of the same magnetic layer, two-dimensional synthetic antiferromagnets, and field-free switching of coupled nanomagnets by spin-orbit torques [28]. Moreover, the intralayer DMI can be used to nucleate and define the position of magnetic domain walls (DWs) [29,30] and realize all-electrical DW logic circuits [10,26,31,32].

Here we show that the intralayer DMI can be used universally to engineer strong, localized intrinsic chiral torques that trigger the spontaneous motion of DWs or bias the speed of current-driven DWs in magnetic racetracks. We first establish a versatile method to characterize the intralayer DMI, which is based on asymmetric DW motion in a benchmark $Pt/Co/AlO_x$ trilayer. We then further extend the method to a $Pt/CoB/AlO_x$ trilayer with low DW pinning, where the intrinsic chiral torque due to

*zhentao.liu@psi.ch
†ales.hrabec@psi.ch

the DMI is utilized to move a DW in the absence of any external force.

II. EFFECTIVE FIELD DUE TO CHIRAL COUPLING ALONG THE EDGE OF THE RACETRACK

The intralayer chiral coupling induced by the interfacial DMI occurs between adjacent regions of the same magnetic layer having in-plane (IP) and out-of-plane (OOP) anisotropy. These regions can be patterned by selective oxidation or ion irradiation [28,33]. As in bulk systems, the DMI favors the orthogonal alignment of neighboring magnetic moments. The simplest IP-OOP element, schematically shown in Fig. 1(a), can attain four possible magnetic configurations: ←⊙, ←⊗, →⊙, and →⊗, where ← and → (⊙ and ⊗) represent the orientation of the magnetization in the IP (OOP) regions. Owing to the presence of DMI in Pt/Co/AlO_x [10,28,34,35], the left-handed ←⊗ and →⊙ configurations have lower energy, and are separated from the ←⊙ and →⊗ high energy states by the energy barrier given by shape anisotropy in the IP element or by the uniaxial anisotropy in the OOP element. To a first approximation, the energy difference between these states is determined by the DMI energy per unit length of a $\pi/2$ DW, $E_{\rm DM} = \pm\pi Dt/2$ [36], where D is the DMI constant and t is the thickness of the ferromagnet. The chiral alignment of IP ($\vec{M}_{\rm IP}$) and OOP ($\vec{M}_{\rm OOP}$) magnetic moments is thus due to a local effective DMI field [29,37]

$$\vec{H}_{\rm DM} = \frac{2D}{\mu_0 M_s}\left(-\frac{\partial m_z}{\partial x}, 0, \frac{\partial m_x}{\partial x}\right), \tag{1}$$

where μ_0 is the vacuum permeability and M_s is the saturation magnetization. m_z and m_x are the z and x components of the normalized magnetization vector with the coordinates defined in Fig. 1(a). In order to observe the spontaneous effect of chiral coupling in such basic elements, the anisotropy has to be low enough that the effective magnetic field can overcome the associated energy barrier. This approach has been used to form spontaneous chiral magnetic textures such as skyrmions and polar vortices, as well as DW injectors, inverters, or logic devices [10,26,28,29,31,32].

To determine the effect of the chiral coupling at the OOP-IP boundary, we propose a method based on asymmetric DW motion. A DW racetrack device is defined in an extended film as a central track with OOP magnetization, surrounded by two narrow parallel IP strips, and extended OOP regions that have a uniform magnetization set by an external magnetic field, as shown in Fig. 1(b). This defines two stable states, where the magnetization in the central track is parallel (⊙⊙⊙) or antiparallel (⊙⊗⊙) to the two external OOP regions. By injecting a DW into the central

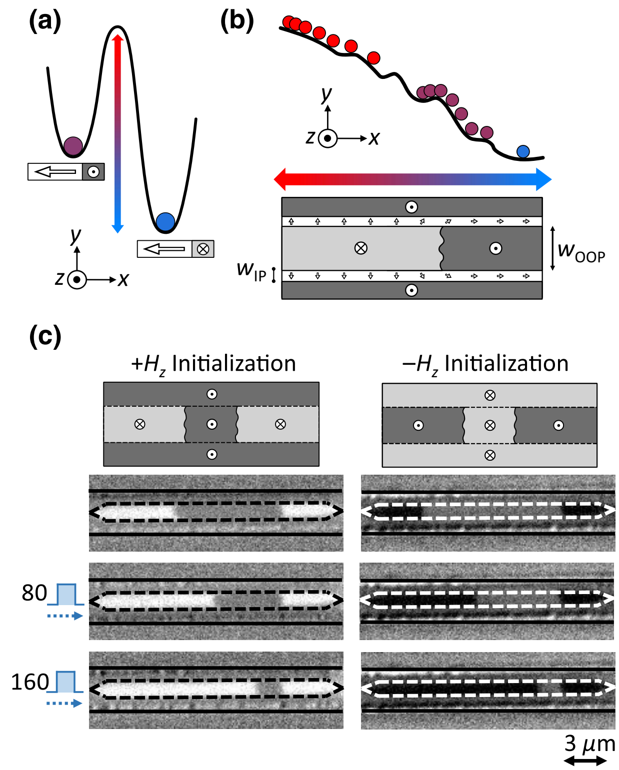

FIG. 1. (a) Schematic of the energy barrier between the unfavorable ←⊙ and favorable ←⊗ chiral configurations of adjacent IP-OOP magnetic regions. The energy barrier between the favorable and unfavorable configuration is given mainly by the shape and uniaxial anisotropies of the IP and OOP regions, respectively. (b) Schematic of a DW racetrack with OOP magnetization delimited by two strips with IP anisotropy. The width of the OOP track and IP strips are $w_{\rm OOP}$ and $w_{\rm IP}$, respectively. The energy landscape of the DW racetrack is monotonic, except for local DW pinning sites, with the slope given by the energy difference between $E_{\odot\odot\odot}$ and $E_{\odot\otimes\odot}$. (c) Sequence of Kerr images of asymmetric DW motion in a racetrack with $w_{\rm OOP}$= 950 nm with corresponding schematics. The dashed lines correspond to the position of the IP magnetized strip whereas the solid lines correspond to the boundary of the magnetic track. Eighty current pulses are applied between each image; the pulse duration is 50 ns and the current density is 3.6×10^{11} A/m^2. The initial magnetic configuration of both inner and outer OOP regions is ⊙ and ⊗ in the left and right panel, respectively.

track, the energy of the system varies with the DW position along the track, as schematically shown in Fig. 1(b), since the chiral coupling across the IP strips favors a track magnetization antiparallel to that of the OOP extended regions (i.e., ⊙⊗⊙ state). This situation can be represented (see Appendix for the detailed model) by an OOP effective driving field

$$H_{\rm eff} = \frac{E_{\odot\otimes\odot} - E_{\odot\odot\odot}}{2\, t\, \mu_0 M_s w_{\rm OOP}}, \tag{2}$$

where $E_{\odot\otimes\odot}$ and $E_{\odot\odot\odot}$ are the linear energy densities of the favorable ($\odot\otimes\odot$) and unfavorable ($\odot\odot\odot$) magnetic states, w_{OOP} is the width of the central track and t is the thickness of the ferromagnetic layer. Since $E_{\odot\otimes\odot} < E_{\odot\odot\odot}$, H_{eff} induces a DW motion in the positive x direction as shown in Fig. 1(b). This effective field is thus due to the energy gradient depending on the DW position along the track. Moreover, in addition to the chiral coupling at the track edges, the energy difference between the $E_{\odot\odot\odot}$ and $E_{\odot\otimes\odot}$ states also results from the dipolar energy (flux closure between the extended OOP regions and the track). The two effects can be distinguished based on their different dependence on the track width. The chiral coupling at the track edges is a local effect that does not depend on the track width, and therefore H_{eff} scales as $1/w_{\mathrm{OOP}}$. In contrast, the dipolar coupling increases with the track width, and therefore H_{eff} should decrease more slowly than $1/w_{\mathrm{OOP}}$ [38]. In the structures investigated here, we find that, depending on the magnitude of the DMI and the thickness, the effects play different roles: for Pt/Co/AlO_x, the DMI is the dominating effect, whereas both effects contribute substantially in Pt/CoB/AlO_x trilayers.

We experimentally investigate this situation in Pt/Co/Al- and Pt/CoB/Al-based samples, where the anisotropy can be tuned by a local Al oxidation. We use magnetron sputtering and electron beam lithography to deposit and pattern a Pt(5 nm)/Co(1.6 nm)/Al(2 nm) multilayer (see Supplemental Material [38] for the fabrication details). The regions with OOP and IP magnetic anisotropy are defined by selective oxidation of the top Al layer through a mask using an oxygen plasma, which protects and defines the regions with IP magnetization. The width of the central track [see Fig. 1(b)] w_{OOP} ranges from 350 to 950 nm, and the width of the IP strips w_{IP} is kept constant at 55 nm.

III. CURRENT-DRIVEN DOMAIN WALL MOTION

In order to reproducibly inject DWs into the track, we create an additional IP V-shaped structure at both ends of the central track [see Fig. 1(c)]. The V-shaped structure facilitates the nucleation of a reversed domain upon current injection [10,31]. To investigate the propagation of DWs in the central track, we first apply a large external OOP magnetic field (±75 mT) to set the magnetic regions in the central DW track and surrounding IP strips to either $\odot$ (with a $+H_z$ field) or $\otimes$ (with a $-H_z$ field), resulting in an unfavorable configuration. This is followed by a sequence of current pulses to nucleate the DWs at the ends of the central racetrack. Then, in order to move the DWs, we apply a series of 50-ns-long current pulses separated by 100 ms. The current density is varied from 1.5×10^{11} to 4×10^{11} A/m^2, and the current polarity determines the

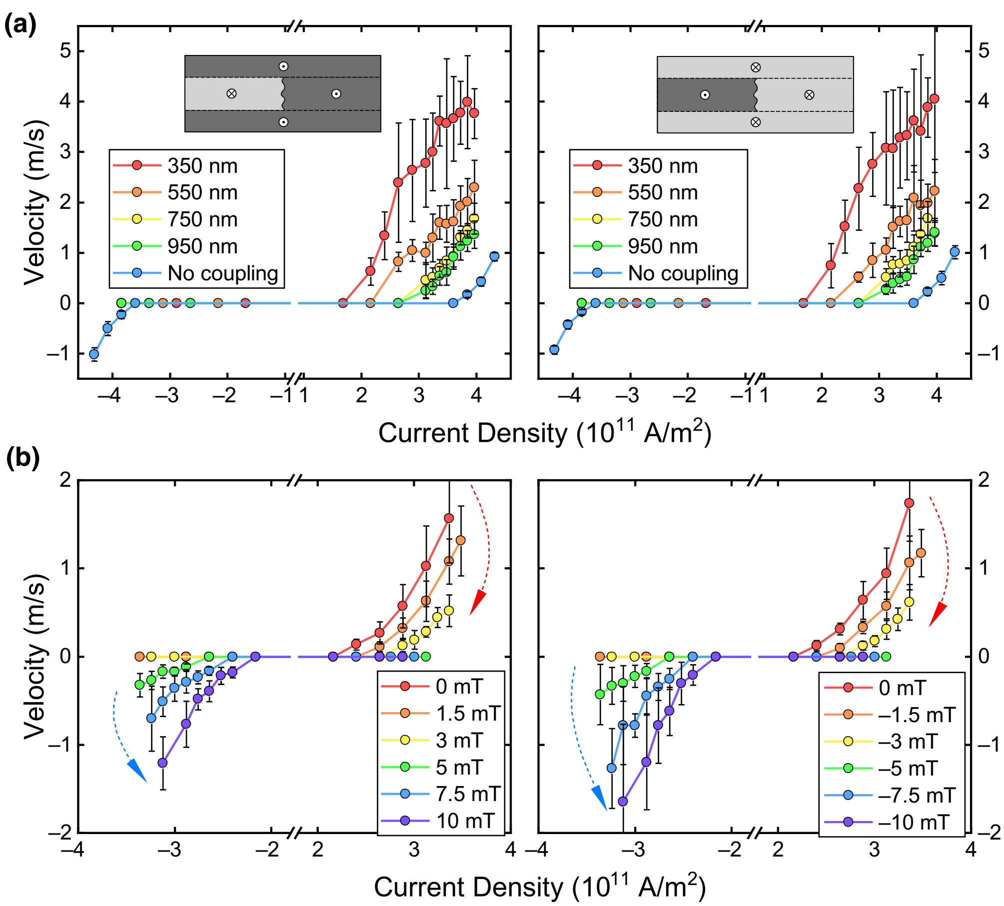

FIG. 2. (a) DW velocity as function of current density for DW tracks with fixed $w_{\mathrm{IP}} = 55$ nm and w_{OOP} ranging from 350 to 950 nm with $+H_z$ initialization (left panel) and $-H_z$ initialization (right panel). The lines are guides to the eye. The error bars are standard deviations for ten individual measurements. (b) Current-induced DW velocity for different values of the OOP magnetic field H_z. The red and blue arrows show the trend of suppressing and enhancing the DW velocity with increasing field, respectively.

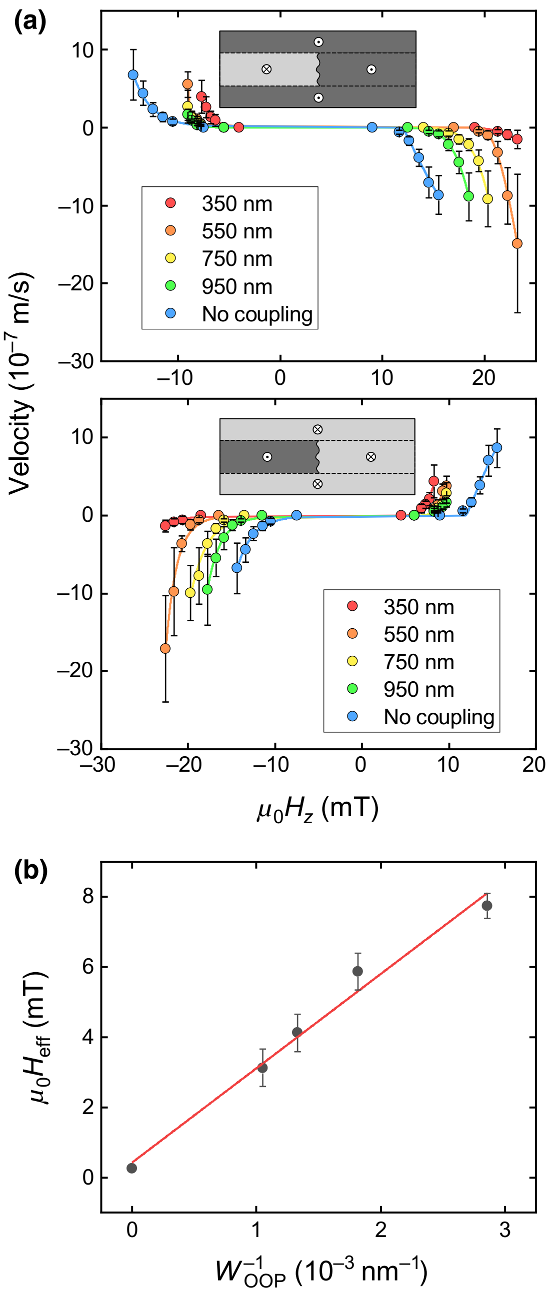

FIG. 3. (a) DW velocity induced by an OOP field H_z measured in Pt/Co/AlO_x devices with w_{IP} = 55 nm and for various w_{OOP} with $+H_z$ initialization (upper panel) and $-H_z$ initialization (lower panel). Control measurements of a 3-μm-wide DW track without the IP strips are also shown. The lines are fits according to Eq. (3). (b) Effective chiral coupling strength (H_{eff}) derived from the creep model. The red line is a linear fit with respect to $1/w_{OOP}$. Error bars represent the standard deviation of H_{eff} measured using both positive and negative magnetic fields.

direction of motion of the DWs, which are of Néel type [36,39].

The position of the DW is tracked by polar Kerr microscopy and a set of images of the DW motion in a racetrack with w_{OOP}= 950 nm at a current density of 3.6×10^{11} A/m^2 is shown in Fig. 1(c) after applying a series of current pulses along the positive x direction. The DW motion induced by the spin-orbit torques is expected to be the same for both ⊙|⊗ and ⊗|⊙ DWs (up-down and down-up mobile DWs); in other words, both the magnitude and sign of the DW displacement for a given polarity of the current should be equal in the absence of external fields [36,40,41]. However, a clear asymmetry is observed in Fig. 1(c) since only the ⊗|⊙ DW (⊙|⊗ DW) moves with a positive current and initialization with a with a $+H_z$ field ($-H_z$ field). This is because the DW that moves favors the expansion of the magnetic domain that satisfies the DMI-induced antiferromagnetic alignment between the central OOP track and the outer OOP strips. The other DW remains fixed at this current density because its motion would lead to the expansion of a domain with magnetization parallel to that of the outer OOP region, which is not favorable. We thus conclude that the DMI coupling at the boundaries of the racetrack exerts an effective chiral torque on the DWs, which is the cause of their asymmetric motion.

To probe the dependence of the chiral coupling on the width of the racetrack, we perform a series of measurements of the DW velocity on the current density in tracks with different w_{OOP}, as shown in Fig. 2(a). It can be seen that the DW velocity is strongly asymmetric, and the velocity of the favored DW increases upon narrowing w_{OOP}, as expected due to the increased importance of the edge of the narrower tracks. In addition, we observe no asymmetry in a control experiment performed on a 3-μm-wide racetrack without the IP magnetized strips (w_{IP}= 0). Moreover, because the chiral coupling acts as an effective magnetic field H_{eff} given by Eq. (2), the observed asymmetry can be compensated by applying an external magnetic field. As shown in Fig. 2(b), on applying an OOP magnetic field H_z ranging from 0 to ±10 mT in a track with w_{OOP}= 350 nm, the motion of the mobile DW is gradually suppressed, whereas the velocity of the unfavorable DW increases. The strength of H_{eff} can in principle be estimated to be the value of H_z that gives no difference in DW velocity for positive and negative current. However, this field cannot be reached experimentally due to parasitic domain nucleation at higher fields.

IV. FIELD-DRIVEN DOMAIN WALL MOTION

To quantify H_{eff}, we therefore measure the DW motion due to the magnetic field H_z alone, i.e., without applying an electric current. In Fig. 3(a), measurements of all track widths are shown without and with chiral coupling (w_{IP}= 0 and 55 nm) in the low-field creep regime on applying H_z in pulses of duration between 2 and 50 s. The DW velocity in the track without chiral coupling is symmetric with respect to the field direction, whereas it is asymmetric in

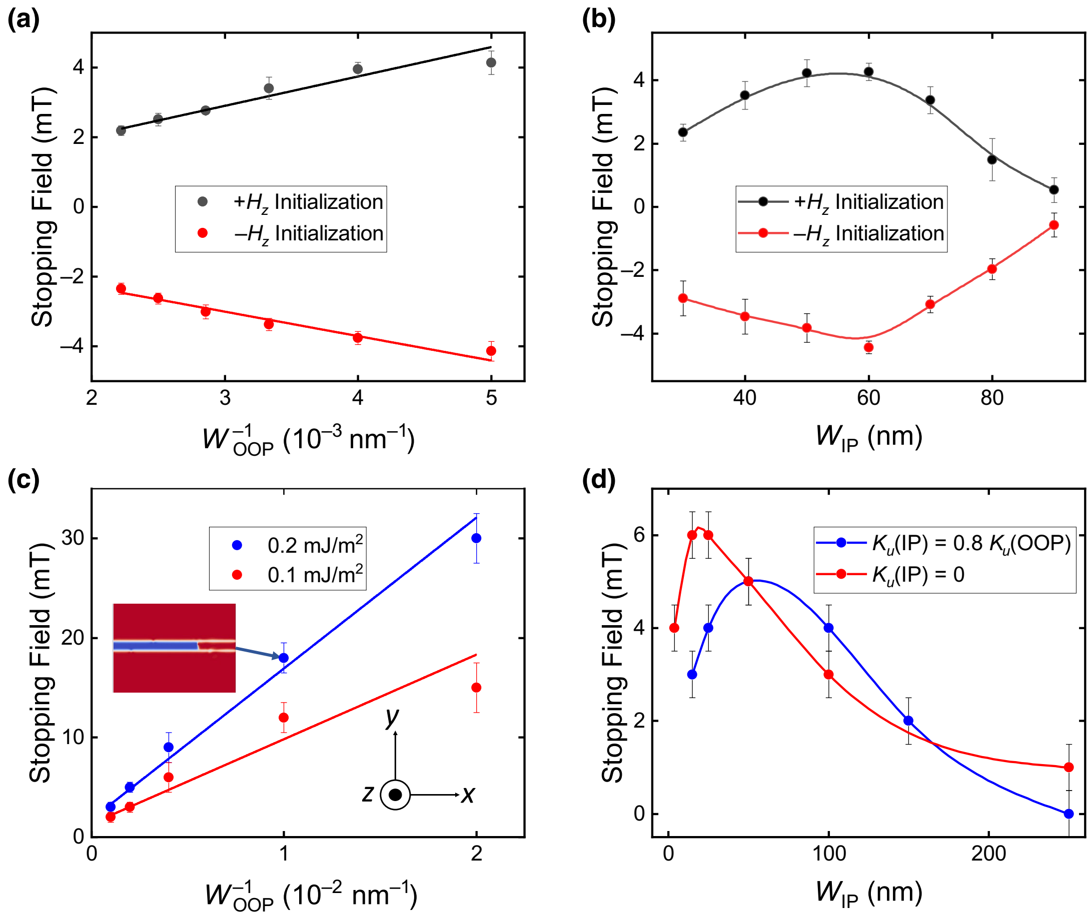

FIG. 4. (a) Stopping field versus $1/w_{\mathrm{OOP}}$ for the DWs in Pt/CoB/AlO_x racetracks with $w_{\mathrm{IP}}=50$ nm. (b) Stopping field in racetracks with $w_{\mathrm{OOP}}=200$ nm and w_{IP} ranging from 30 to 90 nm. (c)–(d) Micromagnetic simulations of the stopping field in a track with a fixed $w_{\mathrm{IP}}=50$ nm and variable $1/w_{\mathrm{OOP}}$ with different interfacial DMI strengths $D=0.1$ and 0.2 mJ/m^2 (c) and in a track with fixed $w_{\mathrm{OOP}}=200$ nm and variable w_{IP} (d) where $D=0.2$ mJ/m^2 with different uniaxial anisotropy constants (K_{u}). The inset in (c) shows a snapshot of the simulations. Red (blue) color corresponds to the OOP magnetization pointing along the +z (−z) direction. The lines in (a) and (c) are linear fits of the stopping field versus $1/w_{\mathrm{OOP}}$, whereas the lines in (b) and (d) are guides to the eye.

the tracks with the IP strips. The asymmetry increases upon increasing the chiral coupling strength by narrowing the track width w_{OOP}. The DW velocity at low magnetic fields generally follows the thermally activated DW creep law [42], which can be expressed as

$$v = v_0 exp\{-\xi[\mu_0 H_z \pm \mu_0 H_{\mathrm{eff}}(w_{\mathrm{OOP}})]^{-1/4}\}, \qquad (3)$$

where v_0 is the characteristic speed and ξ is the scaling coefficient proportional to the thermal energy. The effect of chiral coupling can then be taken into account by adding the DMI effective field $H_{\mathrm{eff}}(w_{\mathrm{OOP}})$ to the external field. By fitting the DW velocity as a function of H_z, we thus find the effective chiral coupling field H_{eff} at different values of w_{OOP}, as shown in Fig. 3(b). The maximum effective DMI field of 7.8 mT corresponds to the minimum $w_{\mathrm{OOP}}=350$ nm. As expected from Eq. (2), we confirm that H_{eff} is inversely proportional to w_{OOP}, as dictated by the local origin of the effective DMI field [28].

V. CHIRAL COUPLING IN Pt/CoB/AlO_x TRILAYER

Although the chiral torque due to H_{eff} has a strong impact on the DW propagation, the torque is not strong enough to induce spontaneous DW motion due to the strong pinning of DWs in Pt/Co/AlO_x. Indeed, it is well known that disorder hinders the DW dynamics by pinning the DWs in Pt/Co films [43–45] and therefore the energy landscape cannot be simply described by Eq. (2) but rather resembles the one sketched in Fig. 1(b). We therefore turn to an alternative material system based on Pt(5 nm)/CoB(4.8 nm)/Al(2 nm), which is known for its

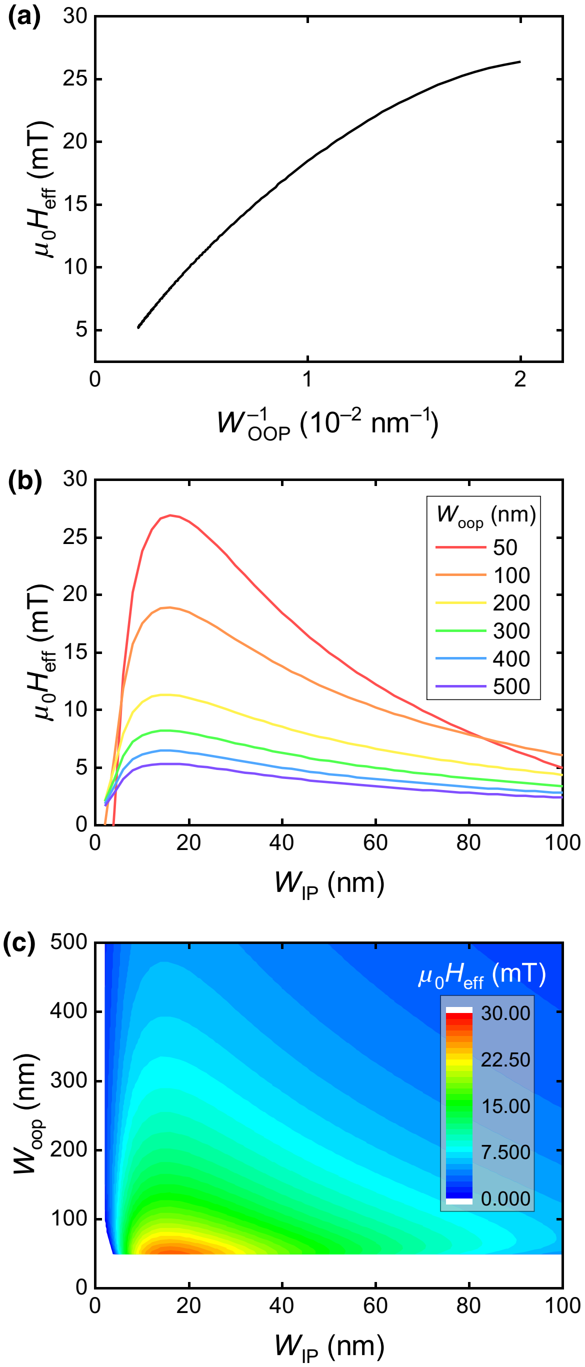

FIG. 5. (a) 1D micromagnetic calculation of H_{eff} versus $1/w_{\mathrm{OOP}}$ in a Pt/CoB/AlO$_x$ racetrack with fixed $w_{\mathrm{IP}} = 20$ nm. H_{eff} is extracted from the calculation of the linear energy density of ⊙⊙⊙ and ⊙⊗⊙ regions using Eq. (2) with $D = 0.2$ mJ/m^2. (b) Simulated H_{eff} as a function of w_{IP} for $w_{\mathrm{OOP}} = 50$ to 500 nm. (c) Color map of H_{eff} versus w_{IP} and w_{OOP}.

low pinning [46–48], and apply the same methodology. IP and OOP magnetized regions are again defined by selective oxidation of the Al capping layer, which changes the magnetic anisotropy of CoB from IP to OOP, as shown in the Supplemental Material [38] (see also Ref. [49]). A similar track design is used to demonstrate the relationship between H_{eff} and w_{OOP} as well as w_{IP}. To examine the effect of the chiral torque due to H_{eff}, the magnetic state of the entire layer is first initialized by applying a magnetic field $H_z = \pm 75$ mT. This results in a high-energy configuration as before, in which the OOP racetrack and the outer OOP region have an ⊙ (⊗) magnetization. As a result of the low pinning and sufficient chiral coupling strength, the DWs start moving before the magnetic field is switched off. Thus, instead of measuring the DW velocity as a function of magnetic field, we measure the so-called stopping field, i.e., the field H_z that compensates H_{eff} (see Supplemental Material [38] and Refs. [50,51] for details). The stopping field is measured by decreasing H_z to zero after saturation in steps of 0.1 mT and observing the threshold value of H_z at which the DW motion is arrested. This field is measured for devices with w_{OOP} ranging from 200 to 450 nm with $w_{\mathrm{IP}} = 50$ nm. As shown in Fig. 4(a), the stopping field monotonically increases upon reducing w_{OOP}, up to ±4.2 mT for $w_{\mathrm{OOP}} = 200$ nm. This observation is in qualitative agreement with the proposed model in Eq. (2). Interestingly, the combination of low pinning and large chiral coupling effect leads to a spontaneous DW motion at zero magnetic field.

To investigate the dependence of H_{eff} on the size of the IP magnetized strips, the stopping field is measured in devices with w_{IP} ranging from 30 to 90 nm with a fixed $w_{\mathrm{OOP}} = 200$ nm [see Fig. 4(b)]. In contrast to the case of variable w_{OOP}, the dependence of the stopping field is not monotonic and a maximum field of ±4.4 mT is observed for $w_{\mathrm{IP}} = 60$ nm. We can understand this by considering that, for w_{IP} narrower than 60 nm, the size of the IP track approaches the natural DW width given by the anisotropy and exchange coupling constant, which suppress the chiral coupling strength. For w_{IP} wider than about 60 nm, the coupling is gradually lost because the chiral coupling effect is localized at the OOP/IP interface. To corroborate our findings, we perform micromagnetic simulations of DW propagation in Pt/CoB/AlO$_x$ racetracks using MUMAX3 (see Supplemental Material [38] for details of the simulation parameters). The simulations, performed in the absence of pinning, reproduce the spontaneous motion of DWs in the racetracks that results from the chiral coupling between the magnetization of the inner track and the outer OOP region [see Fig. 4(c)], and a $1/w_{\mathrm{OOP}}$ dependence of stopping field is observed while changing the width of OOP region with DMI constants of 0.1 and 0.2 mJ/m^2. Both experimental [Fig. 4(a)] and simulation data [Fig. 4(c)] show qualitatively the same $1/w_{\mathrm{OOP}}$ dependence. In addition, as highlighted in Fig. 4(d), the maximum stopping field for a given w_{IP} can be reproduced. However, the position of the maximum strongly depends on the amount of the OOP anisotropy present in the IP strip. Such an anisotropy contribution is expected since, despite the magnetization lying in plane, there is still a significant contribution to the anisotropy from the Pt/CoB interface.

To provide more quantitative insight into the magnitude of $H_{\rm eff}$, the energies $E_{\odot\odot\odot}$ and $E_{\odot\otimes\odot}$ are determined from one-dimensional (1D) micromagnetic simulations. We consider a varying magnetic texture across a track with periodic boundary conditions along x and where we vary $w_{\rm OOP}$ and $w_{\rm IP}$. For simplicity, the OOP anisotropy in the IP region is set to zero. As can be seen in Fig. 5(a), $H_{\rm eff}$ does not completely follow the $1/w_{\rm OOP}$ trend for $w_{\rm OOP} > 50$ nm because the dipolar energy also contributes to the effective field (see Supplemental Material [38] for the estimation). We also confirm that $H_{\rm eff}$ attains a maximum value at $w_{\rm IP} \approx 20$ nm for different $w_{\rm OOP}$ [Fig 5(b)], in good agreement with the stopping field calculations. For narrower or wider IP widths $w_{\rm IP}$ the magnitude of $H_{\rm eff}$ drops off for the same reasons as described above. This therefore suggests that the width of the IP region has to be carefully tailored for a given application. A full dependence of $H_{\rm eff}$ on $w_{\rm OOP}$ and $w_{\rm IP}$ in Fig. 5(c) complements the results shown in Figs. 5(a) and 5(b).

VI. CONCLUSION

In conclusion, we show that the intrinsic chiral torques arising from the DMI at the boundary between the OOP and IP regions of Pt/Co/AlO$_x$ and Pt/CoB/AlO$_x$ DW tracks result in strongly asymmetric DW motion affecting both the current- and field-induced dynamics. The effective field $H_{\rm eff}$ corresponding to the chiral torques can be quantified by measuring the DW velocity in the creep regime or the field required to stop the spontaneous motion of DWs driven by the DMI. Our measurements show that $H_{\rm eff}$ can be finely tuned by designing racetracks with different lateral dimensions $w_{\rm OOP}$ and $w_{\rm IP}$. The observation of strong chiral torques in materials with low pinning, such as CoB, makes it possible to manipulate DWs in the absence of external magnetic fields or electric currents. The unidirectional DW motion and the spontaneous DW propagation could be used to accelerate or decelerate DWs in selected regions of a racetrack when driven by a constant electric current as well as to implement the integrate-and-fire process in artificial neuron network applications. These findings open an alternative path to the local engineering of magnetic torques, which could be implemented for DW motion-based neuromorphic devices [52–55] and magnonic devices [56–59].

The data that support this study are available via the Zenodo repository [60].

ACKNOWLEDGMENTS

This project received funding from the Swiss National Science Foundation (Grant Agreements No. 182013 and No. 200020_200465). A.H. was funded by the European Union’s Horizon 2020 research and innovation program under Marie Skłodowska-Curie Grant Agreement No. 794207 (ASIQS). The authors thank Aleksandr Kurenkov for technical support.

APPENDIX: NUMERICAL MODEL OF EFFECTIVE FIELD INDUCED BY THE CHIRAL EDGES

The dynamics of a DW in the system can be obtained from the energy of $\odot\otimes\odot$ and $\odot\odot\odot$ configurations. We consider a case where a central $w_{\rm OOP}$ wide track with perpendicular magnetization is surrounded by two IP magnetized zones with width $w_{\rm IP}$, which are in turn surrounded by perpendicular magnetized zones as depicted in Fig. 6. While the outer zones are saturated along the $\odot$ direction, the central track hosts a DW, which travels along the track (x direction). The outer and central zones are coupled through the IP zones by a chiral interaction and dipolar coupling (the dipolar field flux closure also favors the $\odot\otimes\odot$ state).

The system energy depends on the DW position along x

$$E(x) = E_{\odot\otimes\odot}x + (L - x)E_{\odot\odot\odot} + C_1, \qquad \text{(A1)}$$

where L is the track length and the constant C_1 contains DW position independent terms. $E_{\odot\otimes\odot}$ and $E_{\odot\odot\odot}$ correspond to the micromagnetic energy density integrated along the sample thickness and width (z and y directions) of the $\odot\otimes\odot$ and $\odot\odot\odot$ states (i.e., far from the DW). Since the chiral and dipolar coupling favor the $\odot\otimes\odot$ state, $E_{\odot\otimes\odot} - E_{\odot\odot\odot} < 0$ and the energy is minimized when the DW moves in the positive x direction. The DW experiences a force

$$F = -\frac{dE}{dx} = E_{\odot\odot\odot} - E_{\odot\otimes\odot}, \qquad \text{(A2)}$$

oriented along the positive x direction.

This situation can be compared with the effect of a magnetic field in the absence of chiral coupling. For a perpendicular field H (positive values favor the $\odot$ orientation), the system energy is

$$E_H(x) = 2\mu_0 H M_s w_{\rm OOP} t\, x + C_2, \qquad \text{(A3)}$$

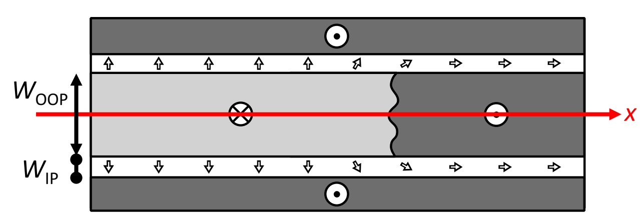

FIG. 6. Sketch of the sample hosting a DW in the central track.

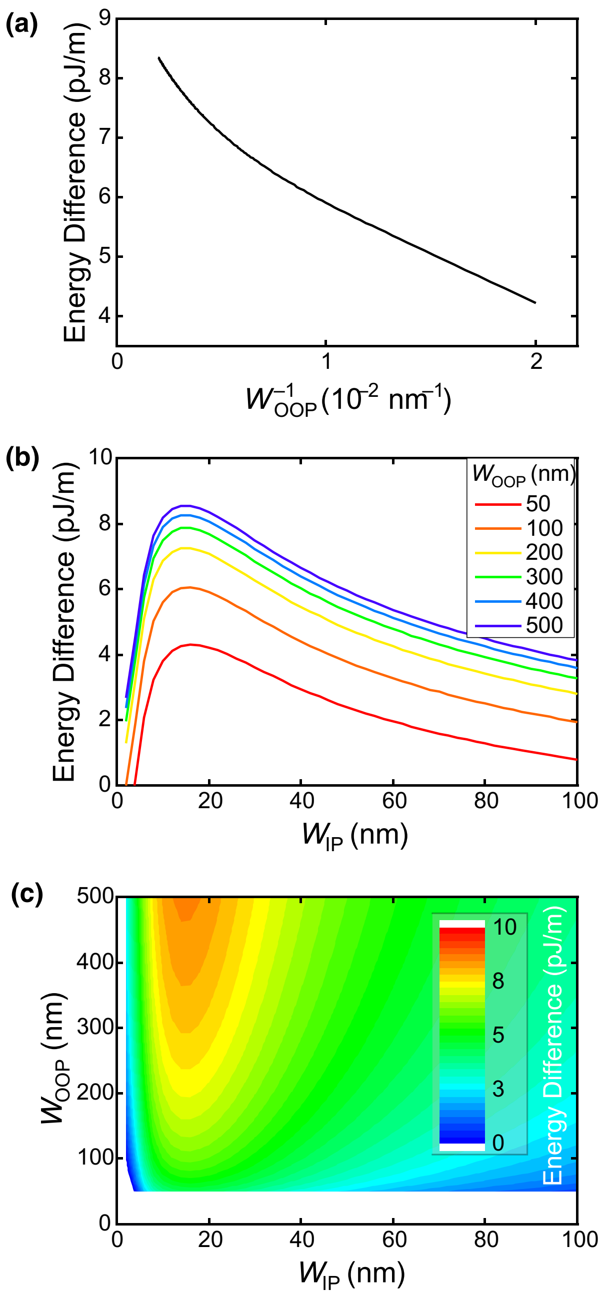

FIG. 7. (a) 1D micromagnetic calculation of energy difference $E_{\odot\odot\odot} - E_{\odot\otimes\odot}$ versus $1/w_{\rm OOP}$ in a Pt/CoB/Al racetrack with fixed $w_{\rm IP}$= 20 nm. (b) Simulated energy difference as a function of $w_{\rm IP}$ for $w_{\rm OOP}$= 50 nm up to 500 nm. (c) Color map of energy difference as a function of $w_{\rm IP}$ and $w_{\rm OOP}$.

where t is the magnetic film thickness and C_2 is another constant independent of the DW position. Note that the factor 2 accounts for the π magnetization rotation in the central track across the DW. The corresponding force is

$$F_H = -2\mu_0 H M_s w_{\rm OOP} t. \tag{A4}$$

Comparing the two forces in Eqs. (A2) and (A4), an effective field, oriented in the $\otimes$ direction, that describes the consequences of chiral edges, is determined as

$$H_{\rm eff} = \frac{E_{\odot\otimes\odot} - E_{\odot\odot\odot}}{2t\mu_0 M_s w_{\rm OOP}}. \tag{A5}$$

This field is negative so it favors the $\otimes$ magnetization orientation in the track and drives the DW along the positive x direction. For the case where the coupling only arises from the DMI, the coupling between the track and the outer zone is purely of the interfacial origin and $E_{\odot\otimes\odot} - E_{\odot\odot\odot}$ is independent of the track width, so the field is inversely proportional to $w_{\rm OOP}$. If dipolar coupling is considered, the flux closure improves as the track width increases so $E_{\odot\otimes\odot} - E_{\odot\odot\odot}$ slightly increases with $w_{\rm OOP}$ and the effective field decreases more slowly than $1/w_{\rm OOP}$. The numerical estimation of the energy difference $E_{\odot\odot\odot} - E_{\odot\otimes\odot}$ in the Pt/CoB/AlO_x trilayer, used to determine the effective fields in Fig. 5, is shown in Fig. 7.

[1] A. Brataas, A. D. Kent, and H. Ohno, Current-induced torques in magnetic materials, Nat. Mater. **11**, 372 (2012).

[2] G. Fuchs, N. Emley, I. Krivorotov, P. Braganca, E. Ryan, S. Kiselev, J. Sankey, D. Ralph, R. Buhrman, and J. Katine, Spin-transfer effects in nanoscale magnetic tunnel junctions, Appl. Phys. Lett. **85**, 1205 (2004).

[3] A. Manchon, J. Železný, I. M. Miron, T. Jungwirth, J. Sinova, A. Thiaville, K. Garello, and P. Gambardella, Current-induced spin-orbit torques in ferromagnetic and antiferromagnetic systems, Rev. Mod. Phys. **91**, 035004 (2019).

[4] E. Grimaldi, V. Krizakova, G. Sala, F. Yasin, S. Couet, G. S. Kar, K. Garello, and P. Gambardella, Single-shot dynamics of spin–orbit torque and spin transfer torque switching in three-terminal magnetic tunnel junctions, Nat. Nanotech. **15**, 111 (2020).

[5] S. S. Parkin, M. Hayashi, and L. Thomas, Magnetic domain-wall racetrack memory, Science **320**, 190 (2008).

[6] P. Grünberg, R. Schreiber, Y. Pang, M. Brodsky, and H. Sowers, Layered Magnetic Structures: Evidence for Antiferromagnetic Coupling of Fe Layers Across Cr Interlayers, Phys. Rev. Lett. **57**, 2442 (1986).

[7] D. A. Allwood, G. Xiong, C. Faulkner, D. Atkinson, D. Petit, and R. Cowburn, Magnetic domain-wall logic, Science **309**, 1688 (2005).

[8] J. A. Currivan-Incorvia, S. Siddiqui, S. Dutta, E. R. Evarts, J. Zhang, D. Bono, C. Ross, and M. Baldo, Logic circuit prototypes for three-terminal magnetic tunnel junctions with mobile domain walls, Nat. Commun. **7**, 1 (2016).

[9] A. Imre, G. Csaba, L. Ji, A. Orlov, G. Bernstein, and W. Porod, Majority logic gate for magnetic quantum-dot cellular automata, Science **311**, 205 (2006).

[10] Z. Luo, A. Hrabec, T. P. Dao, G. Sala, S. Finizio, J. Feng, S. Mayr, J. Raabe, P. Gambardella, and L. J. Heyderman, Current-driven magnetic domain-wall logic, Nature **579**, 214 (2020).

[11] S. Li, W. Kang, Y. Huang, X. Zhang, Y. Zhou, and W. Zhao, Magnetic skyrmion-based artificial neuron device, Nanotechnology **28**, 31LT01 (2017).

[12] J. Grollier, D. Querlioz, K. Camsari, K. Everschor-Sitte, S. Fukami, and M. D. Stiles, Neuromorphic spintronics, Nat. Electron. **3**, 360 (2020).

[13] K. Yue, Y. Liu, R. K. Lake, and A. C. Parker, A brain-plausible neuromorphic on-the-fly learning system implemented with magnetic domain wall analog memristors, Sci. Adv. **5**, eaau8170 (2019).

[14] M. D. Stiles, Interlayer exchange coupling, J. Magn. Magn. Mater. **200**, 322 (1999).

[15] J. Nogués, J. Sort, V. Langlais, V. Skumryev, S. Suriñach, J. Muñoz, and M. Baró, Exchange bias in nanostructures, Phys. Rep. **422**, 65 (2005).

[16] E. E. Fullerton, J. Jiang, and S. Bader, Hard/soft magnetic heterostructures: Model exchange-spring magnets, J. Magn. Magn. Mater. **200**, 392 (1999).

[17] L. Néel, Sur un nouveau mode de couplage entre les aimantations de deux couches minces ferromagnétiques, CR Acad. Sci **255**, 1676 (1962).

[18] B. Dieny, V. S. Speriosu, S. S. Parkin, B. A. Gurney, D. R. Wilhoit, and D. Mauri, Giant magnetoresistive in soft ferromagnetic multilayers, Phys. Rev. B **43**, 1297 (1991).

[19] N. Perrissin, S. Lequeux, N. Strelkov, A. Chavent, L. Vila, L. D. Buda-Prejbeanu, S. Auffret, R. C. Sousa, I. L. Prejbeanu, and B. Dieny, A highly thermally stable sub-20 nm magnetic random-access memory based on perpendicular shape anisotropy, Nanoscale **10**, 12187 (2018).

[20] G. Chen, A. Mascaraque, A. T. N'Diaye, and A. K. Schmid, Room temperature skyrmion ground state stabilized through interlayer exchange coupling, Appl. Phys. Lett. **106**, 242404 (2015).

[21] S.-H. Yang, K.-S. Ryu, and S. Parkin, Domain-wall velocities of up to 750 m s− 1 driven by exchange-coupling torque in synthetic antiferromagnets, Nat. Nanotech. **10**, 221 (2015).

[22] Y.-C. Lau, D. Betto, K. Rode, J. Coey, and P. Stamenov, Spin–orbit torque switching without an external field Using interlayer exchange coupling, Nat. Nanotech. **11**, 758 (2016).

[23] A. van den Brink, G. Vermijs, A. Solignac, J. Koo, J. T. Kohlhepp, H. J. Swagten, and B. Koopmans, Field-free magnetization reversal by spin-Hall effect and exchange bias, Nat. Commun. **7**, 1 (2016).

[24] J. Yu, D. Bang, R. Mishra, R. Ramaswamy, J. H. Oh, H.-J. Park, Y. Jeong, P. Van Thach, D.-K. Lee, G. Go, *et al.*, Long spin coherence length and bulk-like spin–orbit torque in ferrimagnetic multilayers, Nat. Mater. **18**, 29 (2019).

[25] V. Krizakova, K. Garello, E. Grimaldi, G. S. Kar, and P. Gambardella, Field-free switching of magnetic tunnel junctions driven by spin–orbit torques at sub-ns timescales, Appl. Phys. Lett. **116**, 232406 (2020).

[26] A. Hrabec, Z. Luo, L. J. Heyderman, and P. Gambardella, Synthetic chiral magnets promoted by the Dzyaloshinskii–Moriya interaction, Appl. Phys. Lett. **117**, 130503 (2020).

[27] S. H. Skjærvø, C. H. Marrows, R. L. Stamps, and L. J. Heyderman, Advances in artificial spin ice, Nat. Rev. Phys. **2**, 13 (2020).

[28] Z. Luo, T. P. Dao, A. Hrabec, J. Vijayakumar, A. Kleibert, M. Baumgartner, E. Kirk, J. Cui, T. Savchenko, G. Krishnaswamy, *et al.*, Chirally coupled nanomagnets, Science **363**, 1435 (2019).

[29] T. P. Dao, M. Müller, Z. Luo, M. Baumgartner, A. Hrabec, L. J. Heyderman, and P. Gambardella, Chiral domain wall injector driven by spin–orbit torques, Nano Lett. **19**, 5930 (2019).

[30] J. H. Franken, M. Herps, H. J. Swagten, and B. Koopmans, Tunable chiral spin texture in magnetic domain-walls, Sci. Rep. **4**, 1 (2014).

[31] Z. Luo, S. Schären, A. Hrabec, T. P. Dao, G. Sala, S. Finizio, J. Feng, S. Mayr, J. Raabe, P. Gambardella, *et al.*, Field-and Current-Driven Magnetic Domain-Wall Inverter and Diode, Phys. Rev. Appl. **15**, 034077 (2021).

[32] Z. Zeng, Z. Luo, L. J. Heyderman, J.-V. Kim, and A. Hrabec, Synchronization of chiral vortex nano-oscillators, Appl. Phys. Lett. **118**, 222405 (2021).

[33] T. Devolder, J. Ferré, C. Chappert, H. Bernas, J.-P. Jamet, and V. Mathet, Magnetic properties of He+-irradiated Pt/Co/Pt ultrathin films, Phys. Rev. B **64**, 064415 (2001).

[34] M. Belmeguenai, J.-P. Adam, Y. Roussigné, S. Eimer, T. Devolder, J.-V. Kim, S. M. Cherif, A. Stashkevich, and A. Thiaville, Interfacial Dzyaloshinskii-Moriya interaction in perpendicularly magnetized Pt/Co/AlO_x ultrathin films measured by Brillouin light spectroscopy, Phys. Rev. B **91**, 180405 (2015).

[35] E. Jué, A. Thiaville, S. Pizzini, J. Miltat, J. Sampaio, L. Buda-Prejbeanu, S. Rohart, J. Vogel, M. Bonfim, O. Boulle, *et al.*, Domain wall dynamics in ultrathin Pt/Co/AlO_x microstrips under large combined magnetic fields, Phys. Rev. B **93**, 014403 (2016).

[36] A. Thiaville, S. Rohart, É Jué, V. Cros, and A. Fert, Dynamics of Dzyaloshinskii domain walls in ultrathin magnetic films, EPL (Europhysics Letters) **100**, 57002 (2012).

[37] S. Rohart and A. Thiaville, Skyrmion confinement in ultrathin film nanostructures in the presence of Dzyaloshinskii-Moriya interaction, Phys. Rev. B **88**, 184422 (2013).

[38] See Supplemental Material at http://link.aps.org/supplemental/10.1103/PhysRevApplied.16.054049 for film deposition; device fabrication; characterization of Pt(5 nm)/CoB(4.8 nm)/Al(2 nm); stopping field in CoB; comparison of Co and CoB system with and without dipolar coupling; and MuMax3 simulation parameters in CoB system.

[39] J.-P. Tetienne, T. Hingant, L. Martínez, S. Rohart, A. Thiaville, L. H. Diez, K. Garcia, J.-P. Adam, J.-V. Kim, J.-F. Roch, *et al.*, The nature of domain walls in ultrathin ferromagnets revealed by scanning nanomagnetometry, Nat. Commun. **6**, 1 (2015).

[40] S. Emori, U. Bauer, S.-M. Ahn, E. Martinez, and G. S. Beach, Current-driven dynamics of chiral ferromagnetic domain walls, Nat. Mater. **12**, 611 (2013).

[41] K.-S. Ryu, L. Thomas, S.-H. Yang, and S. Parkin, Chiral spin torque at magnetic domain walls, Nat. Nanotech. **8**, 527 (2013).

[42] A. Hrabec, N. Porter, A. Wells, M. Benitez, G. Burnell, S. McVitie, D. McGrouther, T. Moore, and C. Marrows, Measuring and tailoring the Dzyaloshinskii-Moriya interaction in perpendicularly magnetized thin films, Phys. Rev. B **90**, 020402 (2014).

[43] P. Metaxas, J. Jamet, A. Mougin, M. Cormier, J. Ferré, V. Baltz, B. Rodmacq, B. Dieny, and R. Stamps, Creep and Flow Regimes of Magnetic Domain-Wall Motion in Ultrathin Pt/Co/Pt Films with Perpendicular Anisotropy, Phys. Rev. Lett. **99**, 217208 (2007).

[44] I. M. Miron, G. Gaudin, S. Auffret, B. Rodmacq, A. Schuhl, S. Pizzini, J. Vogel, and P. Gambardella, Current-driven spin torque induced by the Rashba effect in a ferromagnetic metal layer, Nat. Mater. **9**, 230 (2010).

[45] E. Jué, C. Safeer, M. Drouard, A. Lopez, P. Balint, L. Buda-Prejbeanu, O. Boulle, S. Auffret, A. Schuhl, A. Manchon, *et al.*, Chiral damping of magnetic domain walls, Nat. Mater. **15**, 272 (2016).

[46] R. Lavrijsen, G. Malinowski, J. Franken, J. Kohlhepp, H. Swagten, B. Koopmans, M. Czapkiewicz, and T. Stobiecki, Reduced domain wall pinning in ultrathin $Pt/Co_{100-x}B_x/Pt$ with perpendicular magnetic anisotropy, Appl. Phys. Lett. **96**, 022501 (2010).

[47] R. Lavrijsen, M. Verheijen, B. Barcones, J. Kohlhepp, H. Swagten, and B. Koopmans, Enhanced field-driven domain-wall motion in $Pt/Co_{68}B_{32}/Pt$ strips, Appl. Phys. Lett. **98**, 132502 (2011).

[48] F. Büttner, C. Moutafis, A. Bisig, P. Wohlhüter, C. M. Günther, J. Mohanty, J. Geilhufe, M. Schneider, C. v, K. Schmising, S. Schaffert, *et al.*, Magnetic states in low-pinning high-anisotropy material nanostructures suitable for dynamic imaging, Phys. Rev. B **87**, 134422 (2013).

[49] S. Fukami, T. Suzuki, Y. Nakatani, N. Ishiwata, M. Yamanouchi, S. Ikeda, N. Kasai, and H. Ohno, Current-induced domain wall motion in perpendicularly magnetized CoFeB nanowire, Appl. Phys. Lett. **98**, 082504 (2011).

[50] Y. Yoshimura, K.-J. Kim, T. Taniguchi, T. Tono, K. Ueda, R. Hiramatsu, T. Moriyama, K. Yamada, Y. Nakatani, and T. Ono, Soliton-like magnetic domain wall motion induced by the interfacial Dzyaloshinskii–Moriya interaction, Nat. Phys. **12**, 157 (2016).

[51] A. Mougin, M. Cormier, J. Adam, P. Metaxas, and J. Ferré, Domain wall mobility, stability and Walker breakdown in magnetic nanowires, EPL (Europhysics Letters) **78**, 57007 (2007).

[52] S. A. Siddiqui, S. Dutta, A. Tang, L. Liu, C. A. Ross, and M. A. Baldo, Magnetic domain wall based synaptic and activation function generator for neuromorphic accelerators, Nano Lett. **20**, 1033 (2019).

[53] C. Cui, O. G. Akinola, N. Hassan, C. H. Bennett, M. J. Marinella, J. S. Friedman, and J. A. C. Incorvia, Maximized lateral inhibition in paired magnetic domain wall racetracks for neuromorphic computing, Nanotechnology **31**, 294001 (2020).

[54] T. Jin, W. Gan, F. Tan, N. Sernicola, W. S. Lew, and S. Piramanayagam, Synaptic element for neuromorphic computing Using a magnetic domain wall device with synthetic pinning sites, J. Phys. D Appl. Phys. **52**, 445001 (2019).

[55] T. Shibata, T. Shinohara, T. Ashida, M. Ohta, K. Ito, S. Yamada, Y. Terasaki, and T. Sasaki, Linear and symmetric conductance response of magnetic domain wall type spin-memristor for analog neuromorphic computing, Appl. Phys. Express **13**, 043004 (2020).

[56] F. Buijnsters, Y. Ferreiros, A. Fasolino, and M. Katsnelson, Chirality-Dependent Transmission of Spin Waves Through Domain Walls, Phys. Rev. Lett. **116**, 147204 (2016).

[57] K. Wagner, A. Kákay, K. Schultheiss, A. Henschke, T. Sebastian, and H. Schultheiss, Magnetic domain walls as reconfigurable spin-wave nanochannels, Nat. Nanotech. **11**, 432 (2016).

[58] S. J. Hämäläinen, M. Madami, H. Qin, G. Gubbiotti, and S. van Dijken, Control of spin-wave transmission by a programmable domain wall, Nat. Commun. **9**, 1 (2018).

[59] J. Han, P. Zhang, J. T. Hou, S. A. Siddiqui, and L. Liu, Mutual control of coherent spin waves and magnetic domain walls In a magnonic device, Science **366**, 1121 (2019).

[60] Z. Liu, Z. Luo, S. Rohart, L. J. Heyderman, P. Gambardella, and A. Hrabec, Dataset for engineering of intrinsic chiral torques in magnetic thin films based on the Dzyaloshinskii-Moriya interaction, Zenodo. https://doi.org/10.5281/zenodo.5045245